Table 3
Nominal vs. actual material properties.

	Units	Nominal	Actual
Young Modulus	[GPa]	205	205
Poisson Ratio	[-]	0.30	0.30
Yield Strength	[MPa]	355	400
Tensile Strength	[MPa]	455	500
Strain Hardening Modulus	[MPa]	1025	287
Elongation at break	[-]	0.10	0.35

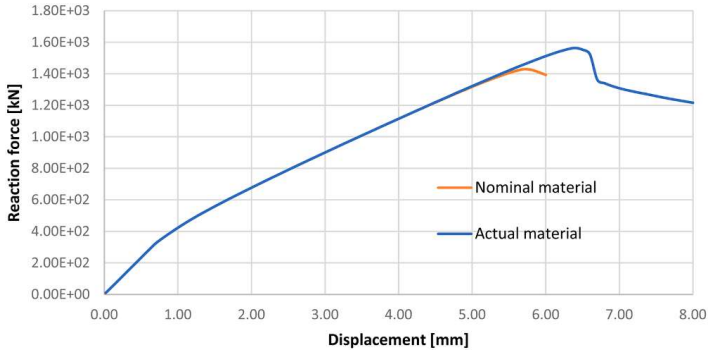

Fig. 10. Load end-shortening curves comparison: nominal vs. actual material properties.

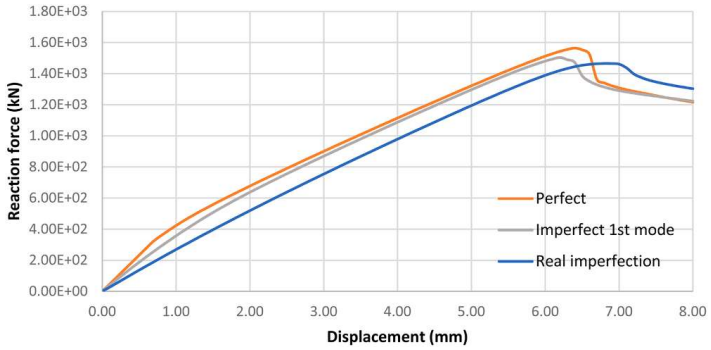

Fig. 11. Load end-shortening curves comparison: perfect and imperfect model.

6.1. *Experimental considerations regarding strain distribution on structural elements*

Fig. 16 depicts the relationship between longitudinal (axial) compressive strain and the applied axial load, as measured by two strain gauges on the shell plating at the same longitudinal position on opposite faces (top and bottom, referred to as A and E strain gauges), and by the strain gauge onto the side longitudinal beam faceplate at the same longitudinal coordinate (referred to as M strain gauge). The difference between the two strain results of the plating is attributed to the local bending effect of the plate, which is also influenced by initial imperfections.

Fig. 12. Panel setup, view from the moving edge which translates axially thanks to the two actuators.

Fig. 13. Load cell heads with ball joint coupling (a) and position of the load cells (b).

Additionally, Fig. 17 demonstrates an almost perfect agreement of measured strain values on the longitudinal beams in all three sections of the panel (strain gauges M, N, O, P), while this consistency is not observed for the axial compressive strains measured onto the plating (Fig. 18). This suggests that the deformation pattern of the plating is highly dependent to the initial imperfections. The visible signal fluctuation in Fig. 17 for the strain gauge "P" on the side beam flange is a result of an electrical disturbance in the measurement chain, which has consequently affected the fluctuation. In order to preserve the original data, it has been decided not to filter the strain measurement of this sensor.

The change in slope on the axial strain measured on the faceplates of side longitudinal beams in the range 100–200 kN is consistent with the phenomena shown in the following Fig. 19, highlighting an increasing contribution in terms of axial stiffness by the shell plating of the panel. This is confirmed also by analysing the fraction of applied load carried by the longitudinal side beams (excluding their effective width) as reconstructed from the strain gage data and reported in Fig. 19 and further described in the following. In the range between 250 and 600 kN of applied compressive load, a higher collaboration of the shell plating is observed.

Strain measurements were utilized to analyse which fraction of the axial force is carried by the longitudinal side girders and which one is instead carried by the plating of the panel, as illustrated in Fig. 19, which is based on data measured from strain gages C, G, K, O, and described in the following.

The nominal axial stiffness of the T section was considered to obtain the acting force based on the strain measurements and similarly the thickness of the plate was used to derive its axial stiffness and corresponding carried force. Specifically, the allocation of carried forces between the plating and the longitudinal side girders was derived by initially computing their cross-section area. Lateral displacement due to initial geometrical imperfection and elastic buckling led to a slight bending deformation on the side girders, which was estimated assuming a linear variation of strain with respect to the lateral coordinate.

Strain gages on webs and faceplate were able to capture this effect, and to achieve an estimation of the axial strain distribution on the beam cross section. Hence, it was possible to compute the normal load carried by beams from measured strain distribution from Eq. (1):

$$Nx = \int_A E\varepsilon_x dA \tag{1}$$

Being Nx the axial force carried by the side beams, excluding its effective width, ε_x the axial strain and E the Young modulus.

It is assumed that the difference between the measured compressive force applied on the panel and the axial force experimentally

Fig. 14. Potentiometric displacement sensor (a) and strain gauge rosette with 3 acquisition channels (0°, 45°, 90°) (b).

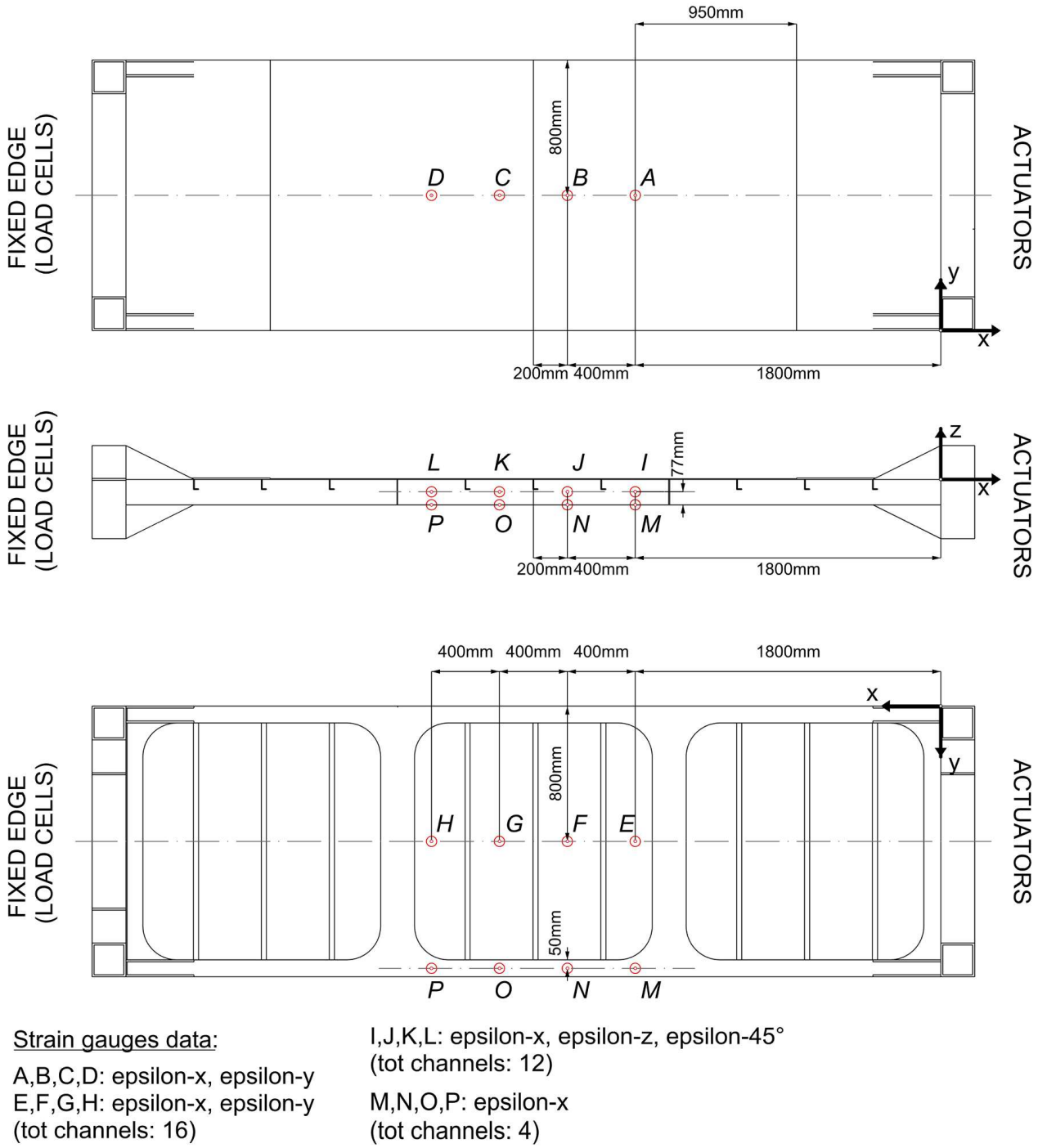

Fig. 15. Strain gauges locations and type.

evaluated by strain gauges data on the longitudinal side beams is carried by the shell plating.

Moreover, strain gages on the panel shell plating allowed the estimation of the complete strain tensor on top and bottom surfaces; hence it was possible to estimate the stress on the shell plating in the central point. It is worth noting that a very good matching is observed in terms of load carried by the panel, as estimated deducting the load on beams from the total compressive force applied and by directing computing the axial force on the shell plating from strain gage data.

Again, in the early stage a lack of the contribution of the plating is observed; thereafter the plating seems to increase collaborating up to carrying the expected fraction of the applied force at 600 kN. Passed this threshold, a higher fraction of the loading is again carried by the side beams, possibly due to a load redistribution due to edge rotations, as shown in Fig. 25.

This phenomenon can be due to a very imperfect pattern of the plating, or alternatively to its early instability, but also to the effects related to welding-induced residual stresses, which is rather complicate to assess owing the limited available fabrication and experimental data and the difficulties in the simulation of the welding process inducing them.

6.2. Modelling of residual stresses

Aiming to roughly assess the effect of residual stresses, the numerical model was updated following the study by Yi et al. [27], which proposes an empirical formulation for predicting welding-induced residual stresses on stiffened panels and provides instructions on how to apply them as initial conditions of a numerical model. The application of these initial conditions implies a numerical model able to distribute the residual stresses on the plating as shown in Fig. 20. This distribution requires a model with a very fine mesh in compliance with the a_t and b_t values, i.e. 10 mm element edge length, in order to be able to apply the residual stresses values as indicated in Fig. 20. The new built-up model surfaces and mesh details are shown in Fig. 21.

From the Yi et al. aforementioned study [27], the extension a_t and b_t of the tensile residual stress zone on the plating can be estimated by numerical/experimental regression formulae as a function of both, the plate slenderness ratios β_x and β_y and the weld bead length L_w:

$$\begin{cases} a_t = \left(-0.6212 \cdot \beta_x^2 + 5.9145 \cdot \beta_x - 3.3894\right) \cdot L_w + 1.9505 \cdot \beta_x^2 - 16.234 \cdot \beta_x + 18.711 \\ b_t = \left(-0.0119 \cdot \beta_y^2 + 0.5177 \cdot \beta_y + 1.1372\right) \cdot L_w + 0.0089 \cdot \beta_y^2 - 0.1506 \cdot \beta_y - 3.1284 \end{cases} \tag{2}$$

After the evaluation of the tensile residual stress zones, it is possible to calculate the magnitude of the compressive residual stresses, considering the tensile ones equal to yielding stress (400 MPa, as per Table 3):

$$\begin{cases} \sigma_{rcx} = \dfrac{2 \cdot b_t}{2 \cdot b_t - b} \cdot \sigma_{rtx} \\ \sigma_{rcy} = \dfrac{2 \cdot a_t}{2 \cdot a_t - a} \cdot \sigma_{rty} \\ \sigma_{rtx} = \sigma_{yield} \\ \sigma_{rty} = \sigma_{yield} \end{cases} \tag{3}$$

For the geometry adopted in the present study, the following analytical residual stress results were obtained, as predicted in [27]:

$$\begin{aligned} \sigma_{rcx} &= -15.02\ MPa \\ \sigma_{rcy} &= -56.91\ MPa \\ \sigma_{rtx} &= 400.00\ MPa \\ \sigma_{rty} &= 400.00\ MPa \end{aligned} \tag{4}$$

The analytical stress field proposed in [27] is imported into the FEM model. In particular, an initial stress field was imposed along the edges of the elementary plate panels surrounded by stiffening members, following a certain spatial distribution. In a first stage of the numerical analyses, the residual stresses were implemented in the FEM model by applying the results of Paik's formulation approximately. In fact, the residual stress distribution was not exactly that suggested in Paik's paper since the abrupt discontinuity is difficult to be implemented in FEA adopting shell element meshes, despite rather refined. Interpolation functions of the elements in way of the discontinuities need to be properly governed and this requires some modelling effort in the adopted software environment.

In a subsequent stage of the work, the Paik's stress field was implemented exactly in the numerical model as shown in Fig. 22a,b, including the abrupt discontinuity at sign change. In Figure 22a stress components σ_{rcy} and σ_{rty} at nodes of the elements along a transverse line on the plating are plotted, while Fig. 22b represents stress components σ_{rcx} and σ_{rtx} at nodes of the elements along the longitudinal central line. Nevertheless, the variation of estimated ultimate collapse load by the nonlinear calculation was negligible in practice, being −0.1 % (Table 4). Hence, confirming that residual stresses have low impact on the ultimate strength of this particular test case.

It is worth remembering that, while in literature mostly collapse tests and numerical analyses of stiffened panels are concerning the case of compressive load applied parallel to ordinary stiffeners, here the load is perpendicular to them. Moreover, a large fraction of the load is carried by the longitudinal side girders rather than by the plating of the panel.

On the other hand, the effect of residual stresses is difficult to exploit as both, tension and compression stresses are summed up onto a stress field of the plating which is evolving during the progressive collapse depending on the local bending behavior of each elementary plate panel surrounded by stiffening members, also influenced by initial geometrical imperfections. Often, residual stresses are accounted for by considering a worst-case scenario.

The introduction of initial residual stresses into the numerical model is not an easy procedure due to nonlinearities. It is important to acknowledge that, even with a relatively refined mesh, the numerical model cannot perfectly replicate the sharp discontinuities in the stress field required by the Yi et al. analytical model (Fig. 20).

As shown in Fig. 23, the obtained residual stresses field does not seem to show a significant impact on the resulting load end-shortening curve if compared to the model completely ignoring residual stresses. Further research is needed to investigate whether the strategy for the application of residual stresses can be improved. Proposed model seems to be reasonable, at least for a rough evaluation of the sensitivity of the numerical model to residual stresses effects, eventually appearing to have minimum impact on the overall structural response.

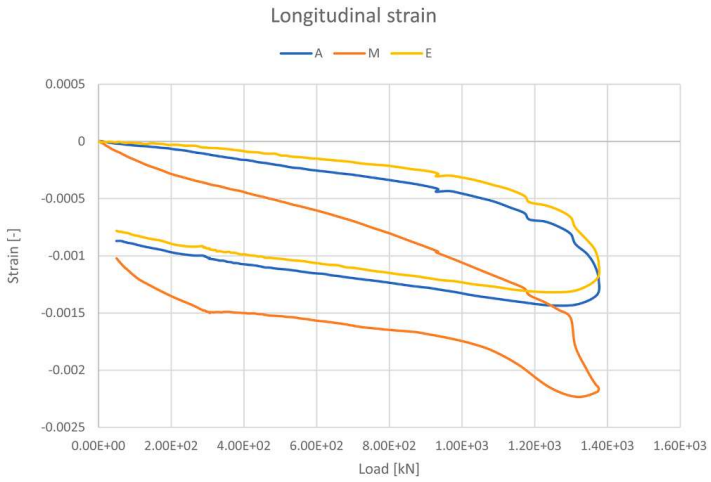

Fig. 16. Longitudinal axial strain gauges results: plating vs longitudinal beam in the same x-coordinate.

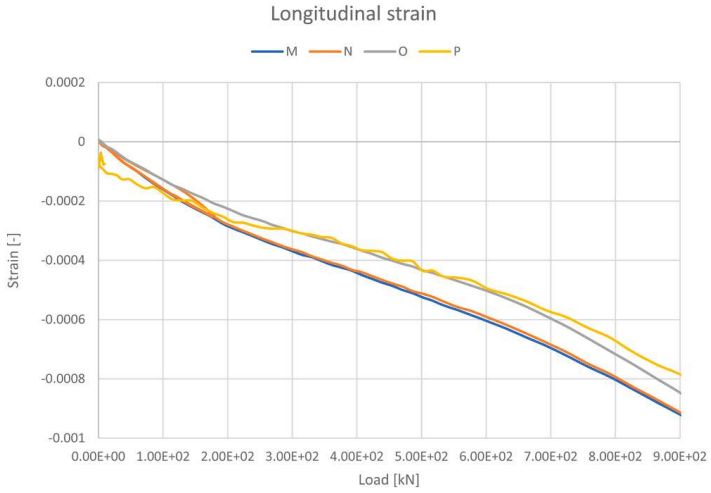

Fig. 17. Load-deformation graph of the longitudinal side beams flanges corresponding to M, N, O, P strain gauges.

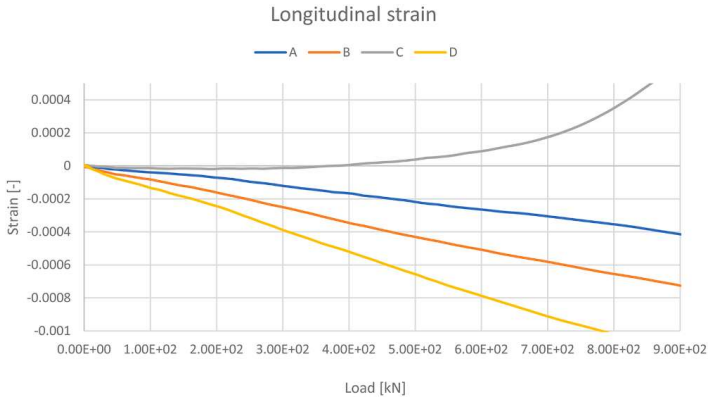

Fig. 18. Load-deformation graph of the plating corresponding to A, B, C, D strain gauges.

7. Experimental/numerical comparison

In this section, the results in terms of load end shortening curves of the perfect numerical model, the imperfect one and the imperfect one with initial residual stresses, are compared with the experimental data (Fig. 23). All results are obtained considering the material properties as shown in Table 2.

From readings of displacement sensors on the actuator side (moving edge in Fig. 12), the vertical end plane of the panel structure

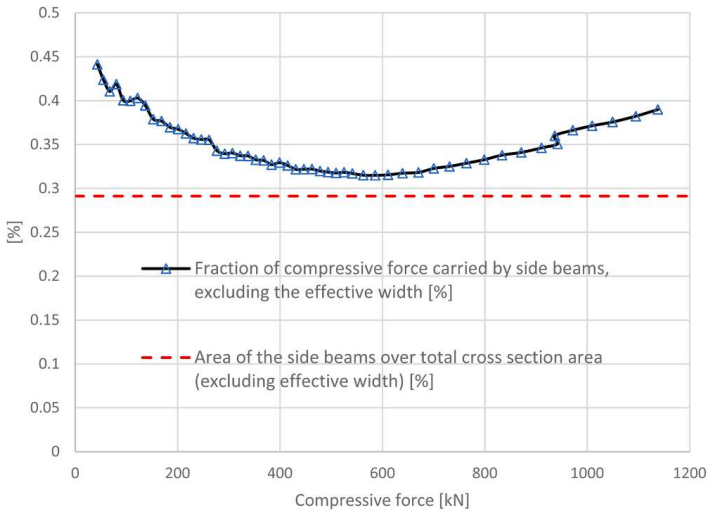

Fig. 19. Sharing of applied load between plating and side girders, as from strain gauges analysis.

was identified. Such plane is in contact with the constraining structures of the testing bench whose stiffness is orders of magnitude larger than that of the specimen panel.

The axial displacement of the rigid link master node was considered in the FEM model (see Fig. 6a). On both ends of the panel, the displacements were considered directly on the specimen to exclude any elastic displacement of the constraint.

In Table 4, the ultimate load values are shown and compared. The table shows that the application of the imperfect shape on the model causes a significant decrease of the ultimate capacity and of the stiffness, while the effect of the residual stresses is almost negligible, maybe due to their low intensity. In fact, the formulations proposed in [27] are analytical-empirical and do not take into account variables related to the production process. Therefore, the obtained result remains uncertain as long as it was not possible to obtain a validation by measuring the actual residual stress directly on the panel before the test.

Residual stresses are incorporated into the FEM model by imposing initial stress conditions and the magnitude of these residual stresses is likely lower in comparison to the existing levels, raising concerns about the significance of results obtained through this method, as they may not accurately reflect actual conditions. As well, integrating the residual stresses into the FEM calculation model as per Yi et al.'s method [27], proves challenging, potentially limiting their overall impact.

From Fig. 23, it is clear that the actual imperfection pattern induces an instant drop of stiffness. It is difficult to explain why the effect is more severe than that observed when considering an initial imperfection that follows the 1st buckling mode shape (see Fig. 11).

The graph shows a pretty good comparison up to about 800 kN of applied axial force, then the specimen seems to become much softer if compared to the numerical prediction. This unexpected phenomenon is also confirmed by the strain gages data, which show that the total axial force carried by the plating does not increase while all the increment in the axial compressive force is carried by the longitudinal side girders only. Such behaviour seems to indicate a local buckling of the plating, with no residual stiffness in the post buckling stage in those structural elements, although local buckling is already observed for a much lower load threshold and confirmed by numerical results showing a drop in the stiffness already on the early stage when actual imperfections are modelled. Further analysis

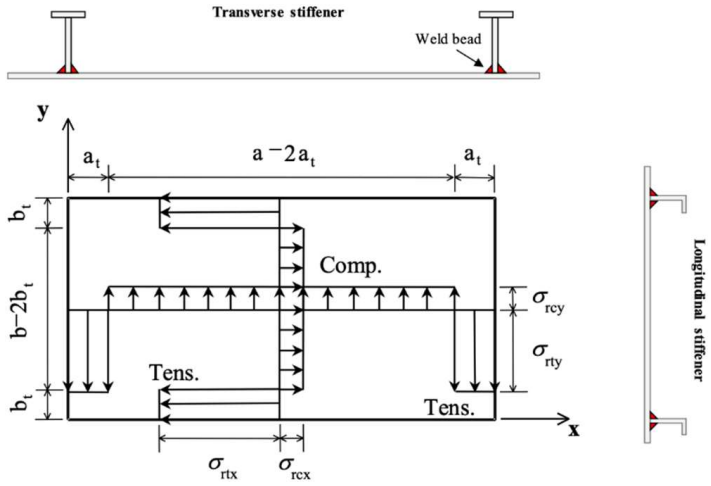

Fig. 20. Distribution of welding-induced residual stresses in stiffened plate structures [27].

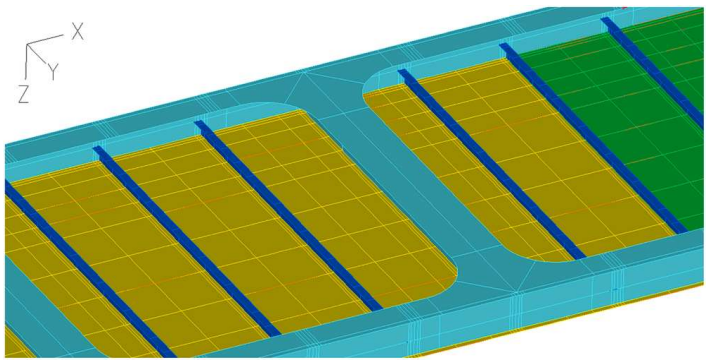

Fig. 21. Detail of the new model geometry.

is needed to investigate if the mismatching could be due, for instance, to a mode snap in the local buckling response.

It is worth noting that also previous experiments of similar setups showed that the experimental end-shortening curve has a smoother response when approaching the ultimate strength and a quite wide plateau in that area is often observed, whereas numerical predictions show a more sudden stiffness loss [2]. It is not completely clear if the smoother experimental response could be due e.g. to boundary conditions that become looser at higher compressive forces. This topic still requires further investigations.

Regarding the displacement discrepancies at the limit state between FEM and experimental results, these can be due to two different sources. The first is the already mentioned residual stresses effect: however, their implementation in the numerical model proposed in this paper do not show significant stiffness variations. The other one is linked to possible displacements of the end constraints: examining displacement data, it seems that a non-negligible rotation of the constrained end of the panel specimen (opposite to the actuators) occurred. Therefore, different constraint conditions are assumed in the numerical model taking advantage of the measurements obtained during the test. The new boundary conditions are set as follows (see Fig. 24):

- Since Load cell #0 indicates a null compressive load, it is considered not in contact. Consequently, the corresponding contact area was left completely free;
- Since load cell #2 recorded the highest load, it is considered perfectly clamped;
- Load cell #1 and load cell #3 are left free to rotate about an axis transverse to the direction of application of the load considering the ball joint coupling as shown in Fig. 13a.

In terms of panel capacity, the correspondence with the experimental ultimate strength is excellent, being the difference only about 0.9 % (Table 4).

Notwithstanding the above, discrepancies between FEM and experimental displacements are still noted. Therefore, as displacement gauges measurements during the experimental test allowed to estimate the rotation of both ends of the panel about the transversal y-axis, an estimate was obtained as shown in Fig. 25.

From this analysis it can be concluded that:

- The rotation of the loaded end of the panel (actuator side) is negligible;
- The rotation of the fixed end does not appear to increase after early stabilization up to a load of about 600 kN, which is close to the global buckling stress on the stiffened panel, as determined by CSR in [18,28] and estimated as 45 MPa, corresponding to an applied load of 568 kN;
- From 600 kN, i.e. the occurrence of global buckling, the fixed end rotation starts to increase constantly, but the global stiffness of the plate does not seem to be significantly affected by the global buckling, and good experimental/numerical agreement is still observed;
- At about 930 kN the support of the first cell (Load cell #0) breaks. The fixed end rotation increases abruptly and the stiffness of the panel starts to decrease. Here, the experimental data start to deviate from the numerical model and, later on, the loss of stiffness is further influenced by the subsequent failure of other supports.

In fact, one of the supports of the load cells was found cracked after the test, likely modifying the boundary condition at the fixed end of the panel. The panel was supposed to be fully constrained against edge rotation in the design stage, hence leading to a bending moment at both ends and null rotations. The geometry was carefully selected in order to minimize the effect of the cross-section centre shift at different cross sections, also including gravity effects in the simulations, to delay effects on global buckling. During the experiment the failure of the cell support altered the boundary conditions at the fixed end of the panel and led to edge rotations.

While the displacement gauges allowed obtaining the modified boundary conditions, it would have been useful to measure the axial displacement field also at different cross-sections, especially in the region of interest for the test, i.e. the central bay of the panel, in order to better reconstruct the exact boundary conditions of that area only.

Finally, the effective (Von Mises) stress and displacement band plots in the ultimate load condition are shown in Figs. 26 and 27. The magnification factor to display the qualitative displacement of the panel is set to 30.

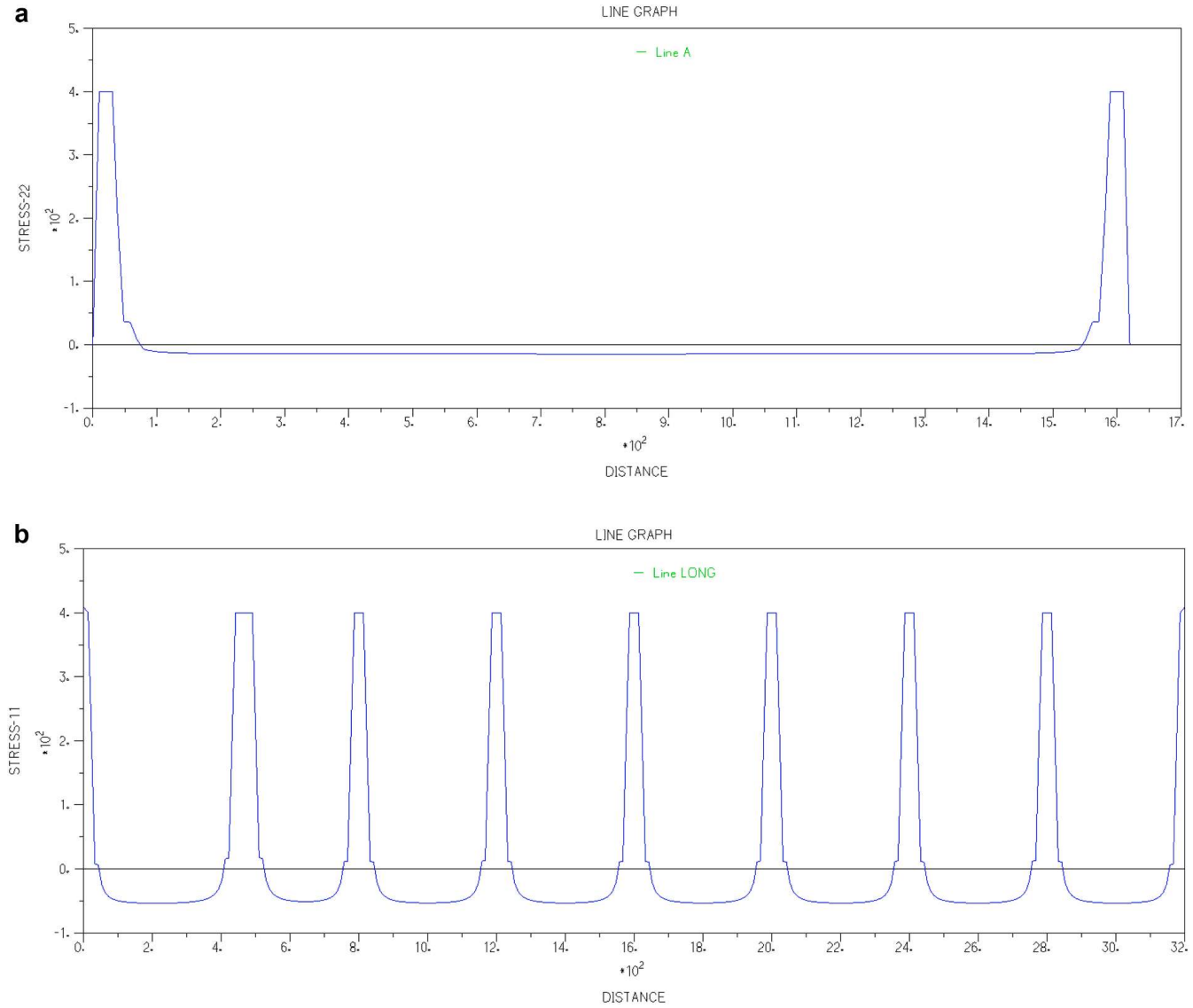

Fig. 22. a: Initial stress field distribution along Y-direction on a transversal line on the plating of the panel.
b: Initial stress field distribution along x-direction on the longitudinal central line on the plating of the panel.

Table 4
Ultimate load values comparison.

MODEL	Ultimate Load [kN]	Ultimate Stress [MPa]	Percentage variation with respect to experimental test [%]
Experimental	1390.3	133.0	–
Perfect – Nominal material properties	1428.5	136.6	+2.7 %
Imperfect - Nominal material properties	1402.5	134.1	+0.9 %
Perfect – Actual material properties	1577.8	150.9	+13.5 %
Imperfect - Actual material properties	1504.7	143.8	+8.2 %
Imperfect + Residual stresses - Actual material properties	1503.0	143.7	+8.1 %
Imperfect+ Res stresses + Modified BC's – Actual material	1377.2	131.7	−0.9 %

Fig. 28a, b shows the post ultimate load condition both in a numerical and experimental way. It can be observed that the numerical model successfully managed to predict the area most affected by the collapse and also the collapse shape. Note that in Fig. 28a the displacement is not scaled, in order to better compare with the experimental (real) one.

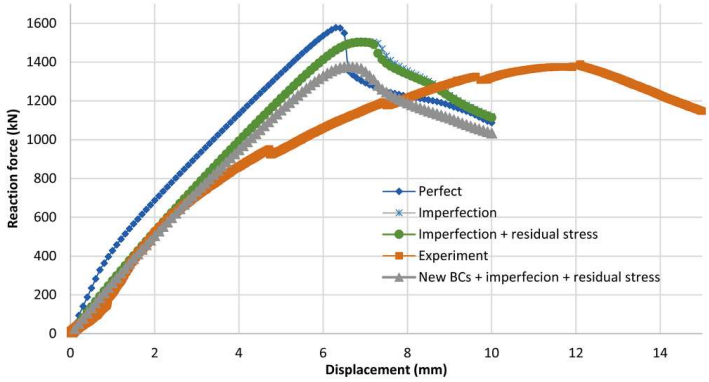

Fig. 23. Load end-shortening curves comparison.

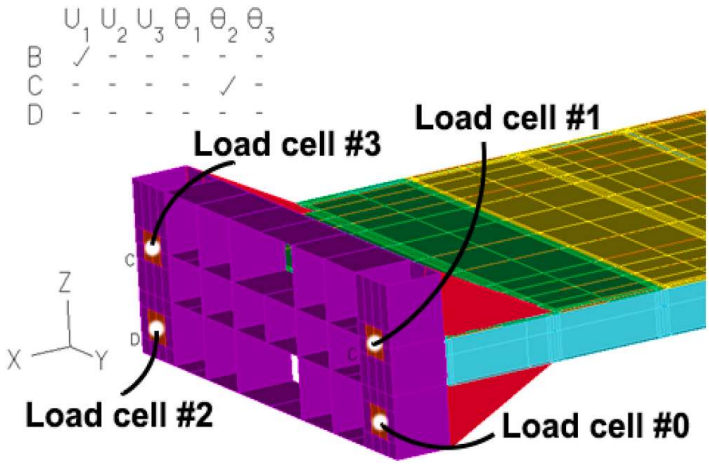

Fig. 24. Modified BC's on the load cells areas (note differences with respect to Fig. 6b).

8. Conclusions

In this work an experimental - numerical comparison of a full-scale test of a ship's structural component was presented. The objective of the test was to estimate the response of the entire structure in the post-buckling phase of the plating of a stiffened panel subjected to transversal compression. The experimental test confirmed a large post buckling response before reaching the ultimate capacity, although highlighting a progressive loss of stiffness of the entire structure.

Major findings of the paper can be summarized as it follows:

- From a finite element simulation perspective, the numerical model was progressively implemented with information regarding the geometric imperfections, measured on the specimen by laser scanners, and the characteristics of the material deriving from tensile

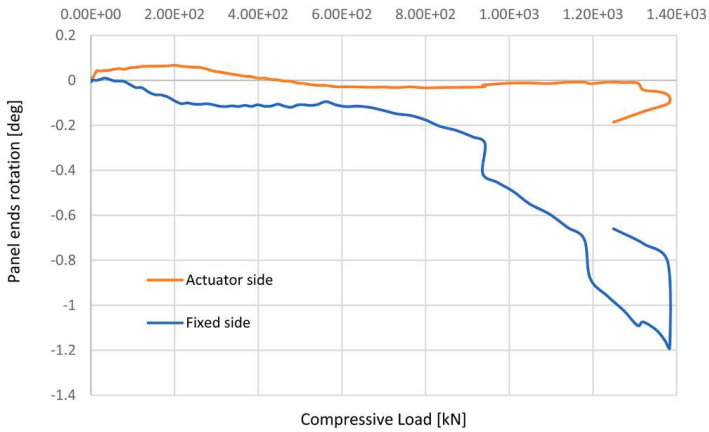

Fig. 25. Experimental rotation at panel ends about the transversal y-axis.

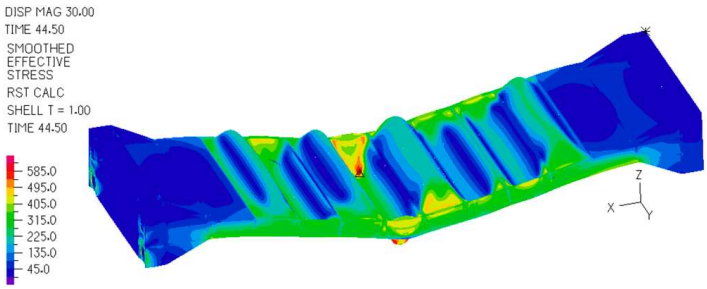

Fig. 26. Von Mises stress distribution [MPa] in the ultimate load condition.

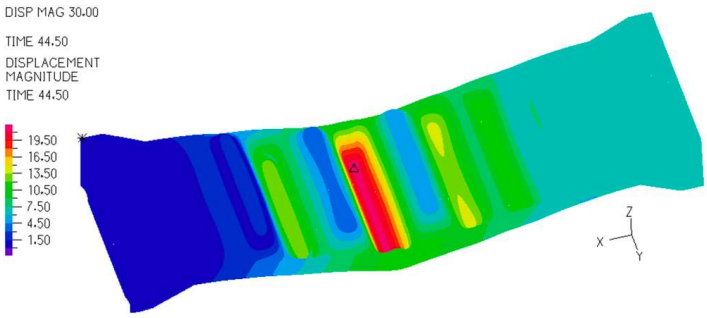

Fig. 27. Displacement magnitude [mm] in the ultimate load condition.

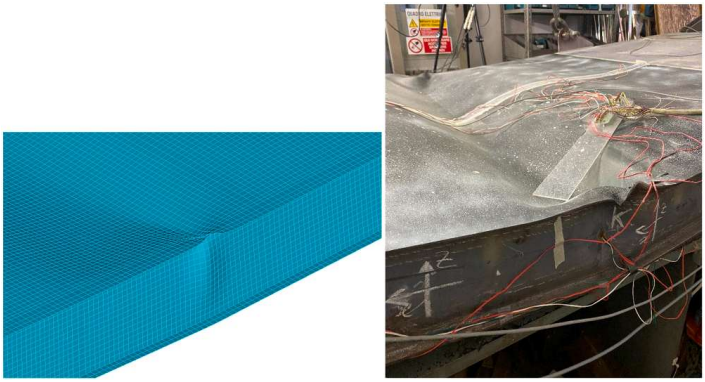

Fig. 28. Comparison between the numerical (a, left) and experimental (b, right) area of collapse.

tests on the same batch of steel plates used to manufacture the specimen. As observed, the correct evaluation of the mechanical properties involves an important variation on the estimate of the ultimate strength of the structure.

- However, the effect of the initial imperfections has led to new questions regarding the actual impact they can have on thin-walled structures subjected to compressive loads. An essential consideration lies in the impact of real imperfections, acquired via laser scanning, which exert a much more substantial influence than the mere approximations of imperfections represented by thin horse shapes or the first buckling mode shape (as depicted in Fig. 10).
- As regards the effect of residual stresses, these have been estimated in an analytical-empirical way following formulations proposed in scientific literature. However, the calculated residual stresses had little influence on the strength and stiffness estimates of the panel numerical model. It's widely acknowledged that these stresses are contingent upon the production process and are challenging to estimate without specialized equipment for experimental detection.
- Considerations on load redistributions were also possible following the analysis of the data acquired by the strain gages, useful to further exploit FEA results in this respect. It came out that the shell plating does not seem to fully collaborate with the side longitudinal girders in the early stage, possibly due to panel buckling in the manufacturing stage caused by residual stress effect, thus impairing the initial overall stiffness of the structural members.

Further investigations are needed to explain the progressive stiffness loss observed in the experiment and not confirmed by numerical analyses. As mentioned before, this can be due to possible displacements of the end constraints. Also, residual stresses evaluation is an aspect to be duly considered in such kind of investigations.

In conclusion, it is noted that the experimental and numerical results described in this paper can be further exploited in the future by the scientific community to support in depth understanding of the collapse of transversally stiffened panel.

CRediT authorship contribution statement

Beatrice Barsotti: Writing – review & editing, Writing – original draft, Visualization, Validation, Software, Methodology, Investigation, Formal analysis, Data curation, Conceptualization. **Carlo Battini:** Writing – review & editing, Software, Methodology, Data curation. **Marco Gaiotti:** Writing – review & editing, Writing – original draft, Visualization, Validation, Supervision, Software, Resources, Project administration, Methodology, Investigation, Formal analysis, Data curation, Conceptualization. **Cesare Mario Rizzo:** Writing – review & editing, Validation, Resources, Project administration, Methodology, Investigation, Funding acquisition, Formal analysis, Data curation, Conceptualization. **Gianmarco Vergassola:** Writing – review & editing, Validation, Software, Methodology, Investigation, Formal analysis, Data curation, Conceptualization.

Declaration of competing interest

The authors declare the following financial interests/personal relationships which may be considered as potential competing interests: Cesare Mario Rizzo reports financial support was provided by Fincantieri Spa. If there are other authors, they declare that they have no known competing financial interests or personal relationships that could have appeared to influence the work reported in this paper.

Acknowledgements

The authors wish to thank Fincantieri Naval Vessels Business Unit, Innovation and Products Development department for funding the experimental activities reported in this paper.

Data availability

Data will be made available on request.

References

[1] Hess PE, et al. In: Proceedings of the 21st international ship and offshore structures congress. III; 2022. Accessed: Aug. 06, 2024. [Online]. Available: http://admin.onepetro.org/snameissc/proceedings-pdf/ISSC22V3/1-ISSC22V3/D011S001R006/3407202/sname-issc-2022-discussion-iii-1.pdf.
[2] Ringsberg JW, et al. The ISSC 2022 committee III.1-Ultimate strength benchmark study on the ultimate limit state analysis of a stiffened plate structure subjected to uniaxial compressive loads. Mar Struct 2021;79. https://doi.org/10.1016/j.marstruc.2021.103026. Sep.
[3] Li S, Benson SD. A re-evaluation of the hull girder shakedown limit states. Sh Offshore Struct 2019;14(sup1):239–50. https://doi.org/10.1080/17445302.2019.1573872. Oct.
[4] Wang Q, Wang D. Ultimate strength envelope of a 10,000TEU large container ship subjected to combined loads: from compartment model to global hull girder. Ocean Eng 2020;213:107767. https://doi.org/10.1016/J.OCEANENG.2020.107767. Oct.
[5] Jagite G, Bigot F, Malenica S, Derbanne Q, Le Sourne H, Cartraud P. Dynamic ultimate strength of a ultra-large container ship subjected to realistic loading scenarios. Mar Struct 2022;84:103197. https://doi.org/10.1016/J.MARSTRUC.2022.103197. Jul.
[6] Fujikubo M, Yao T, Khedmati MR, Harada M, Yanagihara D. Estimation of ultimate strength of continuous stiffened panel under combined transverse thrust and lateral pressure Part 1: continuous plate. Mar Struct 2005;18(5–6):383–410. https://doi.org/10.1016/J.MARSTRUC.2005.08.004. Jul.
[7] Li S, Hu Z, Benson S. An analytical method to predict the buckling and collapse behaviour of plates and stiffened panels under cyclic loading. Eng Struct 2019;199:109627. https://doi.org/10.1016/J.ENGSTRUCT.2019.109627. Nov.
[8] Li S, Hu Z, Benson S. Progressive collapse analysis of ship hull girders subjected to extreme cyclic bending. Mar Struct 2020;73:102803. https://doi.org/10.1016/J.MARSTRUC.2020.102803. Sep.
[9] jie Shi G, yu Wang D, Hu B, Cai SJ. Effect of initial geometric imperfections on dynamic ultimate strength of stiffened plate under axial compression for ship structures. Ocean Eng 2022;256:111448. https://doi.org/10.1016/J.OCEANENG.2022.111448. Jul.
[10] Iijima K, Suzaki Y, Fujikubo M. Scaled model tests for the post-ultimate strength collapse behaviour of a ship's hull girder under whipping loads. Sh Offshore Struct 2015;10(1):31–8. https://doi.org/10.1080/17445302.2013.870774. Jan.
[11] Tabri K, Naar H, Kõrgesaar M. Ultimate strength of ship hull girder with grounding damage. Sh Offshore Struct 2020;15(S1):S161–75. https://doi.org/10.1080/17445302.2020.1827631. Dec.
[12] Li S, Hu ZQ, Benson SD. Ultimate strength performance of a damaged container ship. In: Proceedings of the Royal Institution of Naval Architects – International conference on damaged ship V2020 RINA. Royal Institution of Naval Architects. Royal Institution of Naval Architects; 2020. p. 17–30. Ed.
[13] Georgiadis D, Samuelides M. A methodology for the reassessment of hull-girder ultimate strength of a VLCC tanker based on corrosion model updating. Sh Offshore Struct 2019;14(sup1):270–80. https://doi.org/10.1080/17445302.2019.1577599. Oct.
[14] Guedes Soares C, Gordo JM. Collapse strength of rectangular plates under transverse compression. J Constr Steel Res 1996;36(3):215–34. https://doi.org/10.1016/0143-974X(95)00018-Q. Jan.
[15] Li D, Chen Z. Advanced empirical formulae for the ultimate strength assessment of continuous hull plate under combined biaxial compression and lateral pressure. Eng Struct 2023;285:116041. https://doi.org/10.1016/J.ENGSTRUCT.2023.116041. Jun.
[16] Registro Italiano Navale. Rules for the classification of naval ships RINAMIL. 2017.
[17] Registro Italiano Navale, Rules for the classification of ships. 2023.
[18] International Association of Classification Societies, "Unified Requirements Strength URS-35, Buckling Strength Assessment of Ship Structural Elements," 2024.
[19] Gaiotti M, et al. ISSC 2025 Committee III.1 - Compressive test of a transversely stiffened thin-plated structure with expected early nonlinear response prior to the ultimate capacity. Preliminary comparison of the numerical results. In: Proceedings of the ASME 2024 43rd international conference on ocean, offshore and arctic engineering (OMAE 2024); 2024. p. 1–8. Accessed: Aug. 06, 2024. [Online]. Available: https://research.chalmers.se/en/publication/542139.
[20] DNV-GL, "Class Guideline DNVGL-CG-0128 - Buckling," 2021.
[21] ADINA R&D, Theory and modeling guide, vol. Volume 1. Watertown, USA, 2025.

[22] Barsotti B, Gaiotti M. Cumulative buckling deformation of stiffened panel under cyclic loading. In: Proceedings of the Institution of Mechanical Engineers part M: Journal of Engineering for the Maritime Environment. 238; 2024. p. 375–84. https://doi.org/10.1177/14750902231198902. May.
[23] B. Barsotti, "Ship structure collapse analyses due to non linear effects, with a focus on cyclic loads.," 2024. PhD Thesis, University of Genova (Italy), doi:10.15167/BARSOTTI-BEATRICE_PHD2024-07-03.
[24] Shining 3D, "SHINING3D." Accessed: Aug. 06, 2024. [Online]. Available: https://www.shining3d.com/3d-digitizing-solutions/.
[25] Tanaka S, et al. Evaluation of ultimate strength of stiffened panels under longitudinal thrust. Mar Struct 2014;36:21–50. https://doi.org/10.1016/J.MARSTRUC.2013.11.002. Apr.
[26] International Association of Classification Societies, "Rec.47 - Shipbuilding and Repair Quality Standard, Rev.10," 2021.
[27] Yi MS, Hyun CM, Paik JK. An empirical formulation for predicting welding-induced biaxial compressive residual stresses on steel stiffened plate structures and its application to thermal plate buckling prevention. Sh Offshore Struct 2019;14(sup1):18–33. https://doi.org/10.1080/17445302.2018.1552343. Oct.
[28] International Association of Classification Societies, "Common structural rules for bulk carriers and oil tankers," 2024.